Electronic Supplementary Material (ESI) for Sustainable Energy & Fuels.
This journal is © The Royal Society of Chemistry 2021

Supporting Information

Size-Dependent Selectivity of Iron-Based Electrocatalysts for electrochemical CO_2 reduction

Mengna Xie [a], Na Gao [b,d], GuoPing Xiao [b,c,d], Min Ge [b,c,d], Xian-Long Du* [b,c,d], BingBao Mei [b,c,e], Jian-Qiang Wang [b,c,d] and Tao Li* [a]

[a] Engineering Research Center of Large-Scale Reactor Engineering and Technology, Ministry of Education, State Key Laboratory of Chemical Engineering, East China University of Science and Technology, Shanghai 200237, China

[b] Key Laboratory of Interfacial Physics and Technology, Shanghai Institute of Applied Physics, Chinese Academy of Sciences, Shanghai 201800

[c] University of Chinese Academy of Sciences, Beijing 100049, China

[d] Dalian National Laboratory for Clean Energy, Chinese Academy of Sciences, Dalian 116023, China

[e] Shanghai Synchrotron Radiation Facility, Zhangjiang National Lab, Chinese Academy of Sciences, 201204 Shanghai, China

* Corresponding Author

E-mail: tli@ecust.edu.cn ; duxianlong@sinap.ac.cn

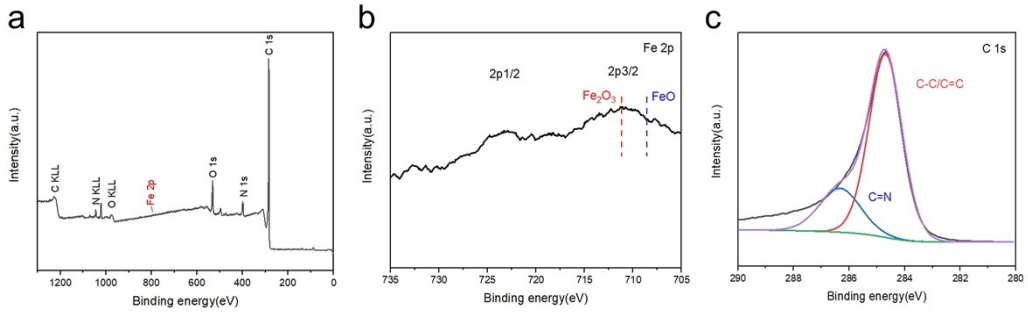

Figure S1. XPS spectra of Fe SAs catalyst. (a) Survey spectra (b) Fe 2p. The red and blue vertical lines indicate the binding energy of Fe $2p^{3/2}$ of Fe_2O_3 and FeO, respectively (c) C 1s

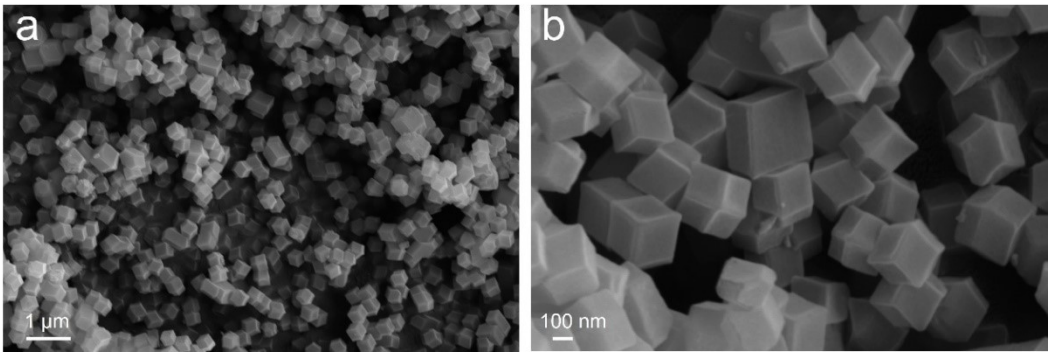

Figure S2. (a) and (b) SEM images of ZIF-8. It is obvious that the synthesized ZIF-8 exhibites a uniform rhombododecahedral shape.

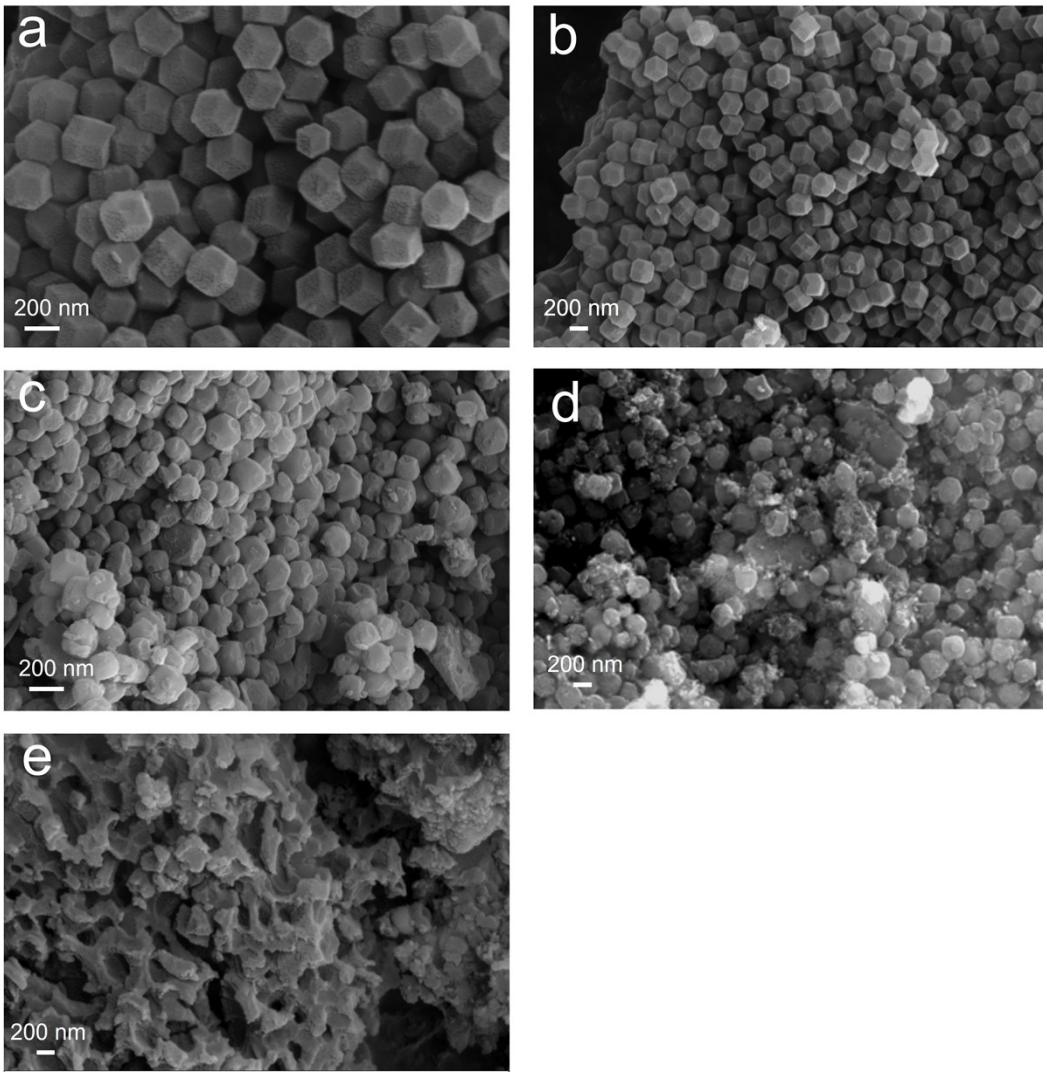

Figure S3. SEM characterization of Fe-N-C. (a) - (e) SEM images of Fe SAs, 7.6 Fe NPs, 16.7 Fe NPs, 44.8 Fe NPs and oversized Fe NPs, which were synthesized by adding 25 μL, 100 μL, 400 μL, 700 μL and 5mL $Fe(NO_3)_3$ solution (100 mg mL^{-1}).

As $Fe(NO_3)_3$ dosage volume increases, the initial rhombic dodecahedron structure collapse gradually and evolves into a porous structure after calcining at 1000°C for 2h.

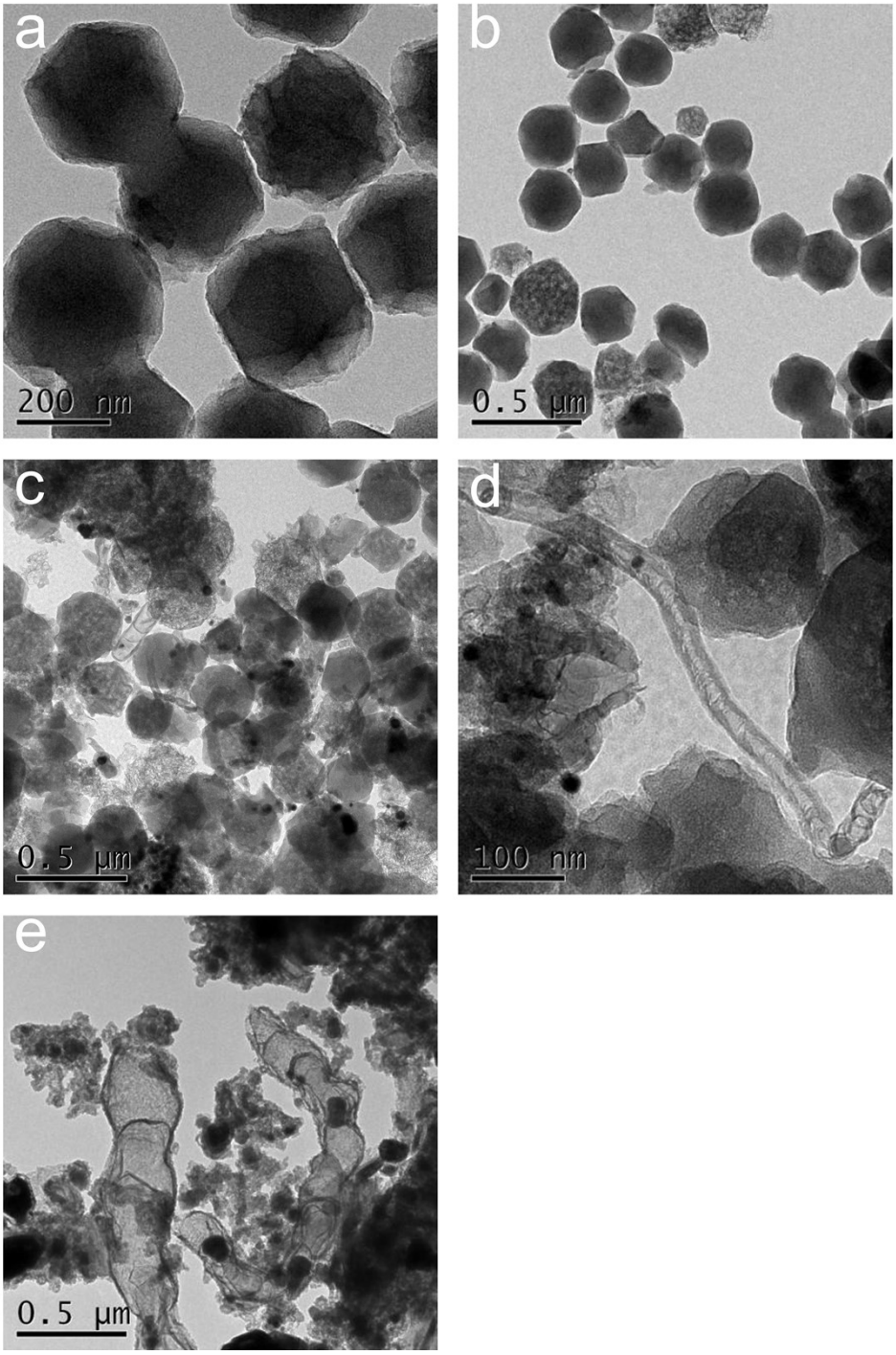

Figure S4. TEM characterization of Fe-N-C. (a) - (e) the representative TEM images of Fe SAs, 7.6 Fe NPs, 16.7 Fe NPs, 44.8 Fe NPs and oversized Fe NPs.

As seen in Figure S3, when increasing the volume of $Fe(NO_3)_3$ solution, carbon nanotubes (CNTs) are formed. The diameter of CNTs is further enlarged from 20-40 nm to 210-300 nm with the specific volume of $Fe(NO_3)_3$ increasing from 400 μL to 5mL, correspondingly.

Generally speaking, metal nanoparticles are commonly utilized as nucleation sites of CNTs, thus the CNTs formed in this experiment may be caused by the nucleation effect of Fe NPs, which comes from the aggregation of Fe SAs.

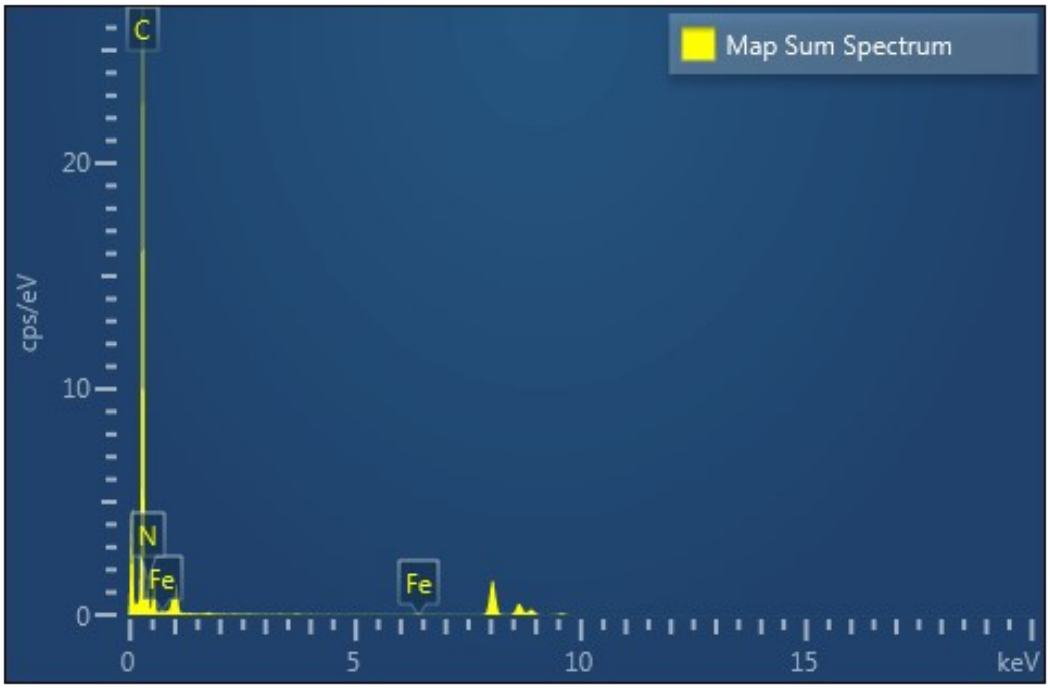

Figure S5. Energy dispersive spectroscopy (EDS) characterization of Fe SAs. No visible Zn signal locating at 8.63 keV was detected in Fe SAs, suggesting low residual Zn content.

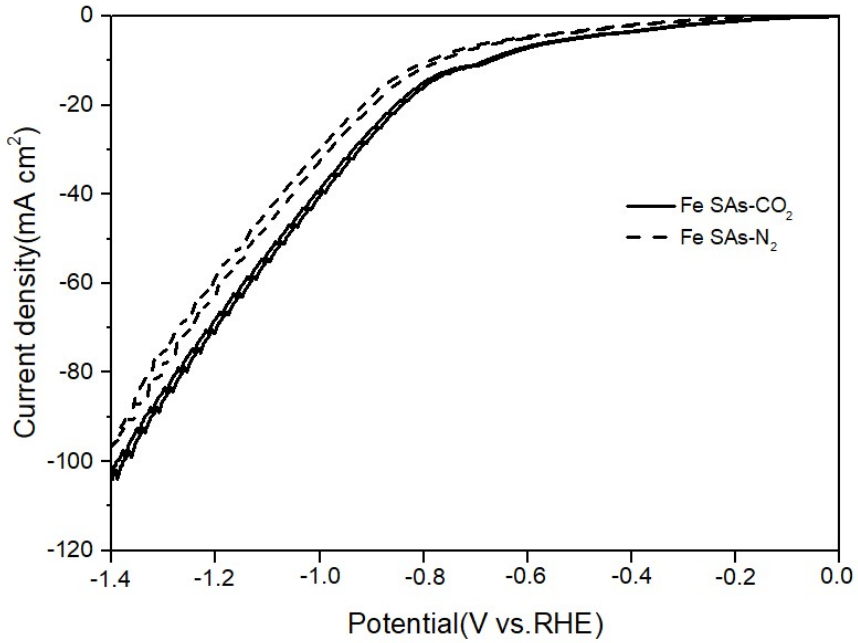

Figure S6. CV curves of Fe SAs, measured in N_2-saturated (dotted line) or CO_2-saturated (solid line) 0.5M $KHCO_3$ within a three-electrode configuration with Pt as the counter electrode and Ag/AgCl as the reference electrode. The test is carried out in a a flow cell with a scanning rate of 10 mV s^{-1}

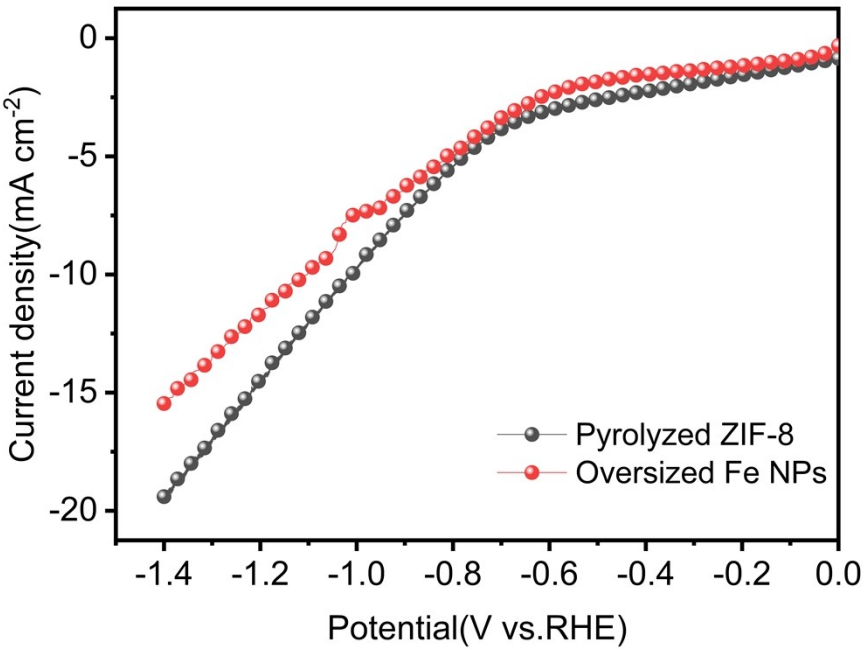

Figure S7. LSV curves of pyrolyzed ZIF-8 and oversized Fe NPs with a scanning rate of 10 mV s^{-1}

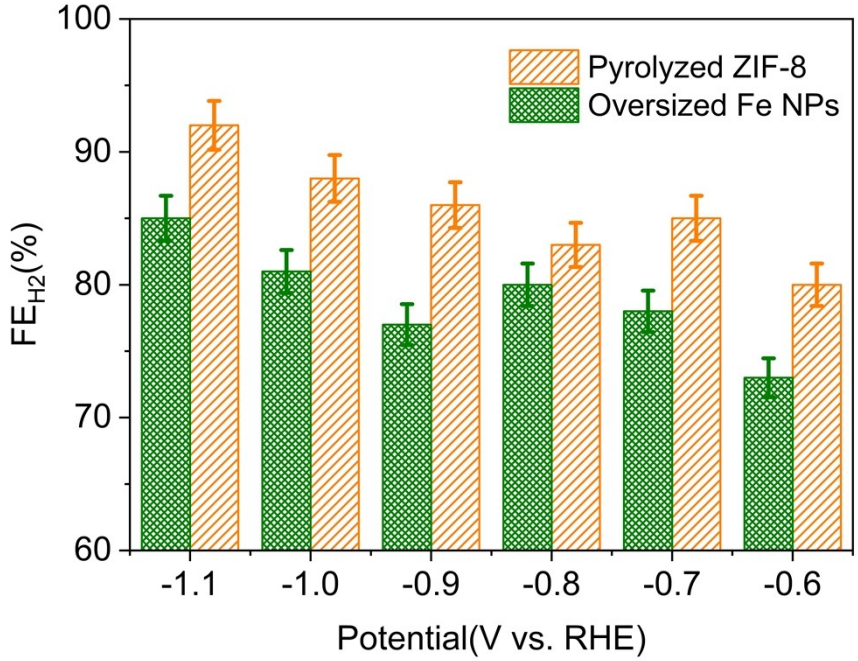

Figure S8. FE for H_2 production of pyrolyzed ZIF-8 and oversized NPs with diameters exceeding 100 nm measured in CO_2-saturated 0.5 M $KHCO_3$.For comparison, N-doped carbon substrate prepared by pyrolysis of ZIF-8 powder without injecting $Fe(NO_3)_3$ solution shows no apparent activity of CO_2RR, whose FE_{H2} is over 80% at all applied potentials, further confirming that the decisive role of isolated iron atoms rather than the N-doped carbon structure in CO_2RR performance. The FE for H_2 production of oversized Fe NPs is also observed to be ~75%, indicating CO_2RR is inhibited while enhancing HER.

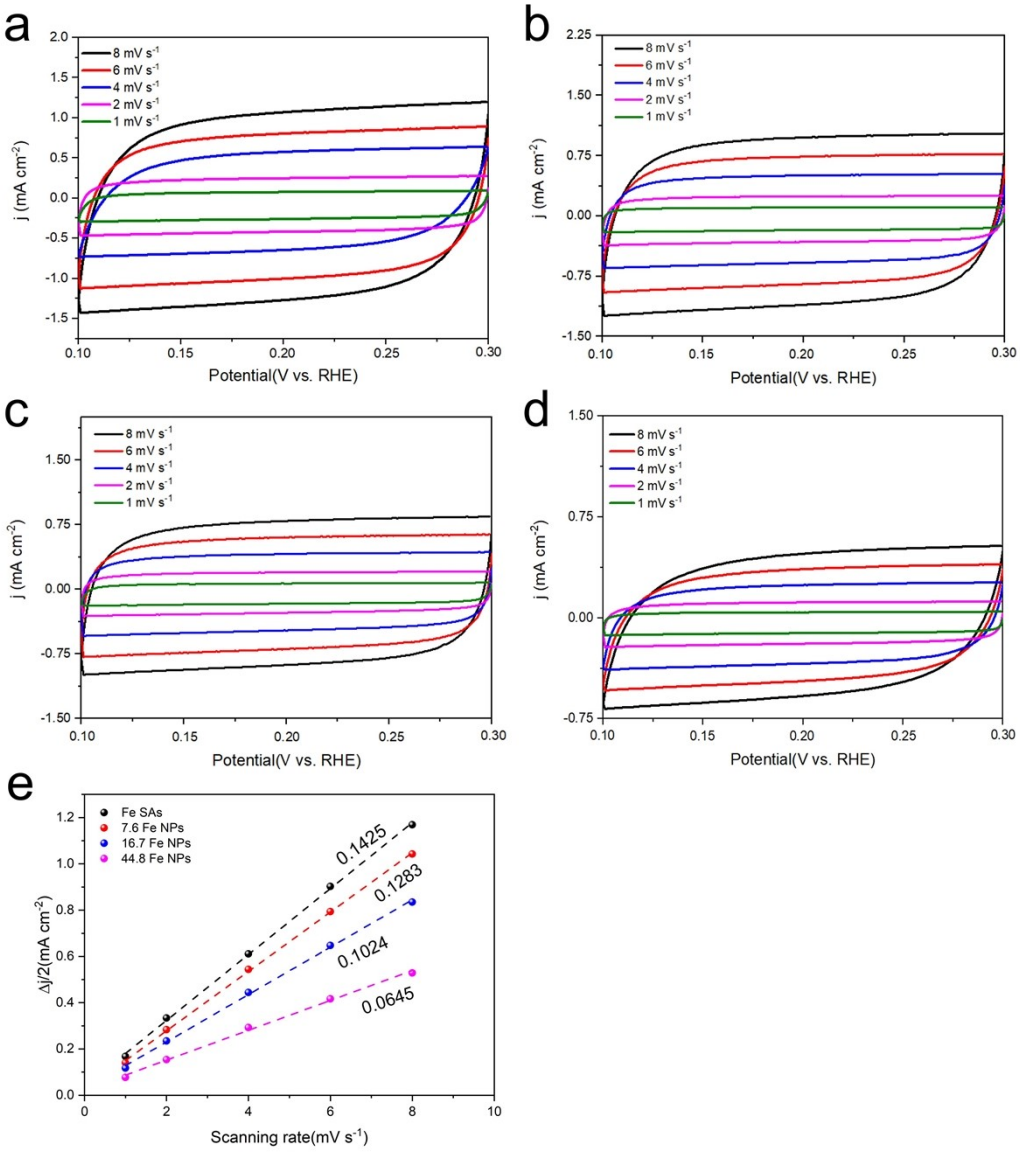

Figure S9. CV curves of (a) Fe SAs, (b) 7.6 Fe NPs, (c) 16.7 Fe NPs and (d) 44.8 Fe NPs. The CV measurements were performed in CO_2-saturated 0.5 M $KHCO_3$ at various scan rates: 1, 2, 4, 6 and 8 mV s^{-1}. (e) A plot of changing current density against scan rates for electrochemically active surface area (ECSA) measurements. As clearly shown, ECSA of the Fe catalysts increased in the following order of Fe SAs > 7.6 Fe NPs > 16.7 Fe NPs > 44.8 Fe NPs, coinciding with the FE_{CO} results

Table S1. Elemental composition of the Ni SA sample detected by EDS

Element	Wt%	Atomic %
C	94.70	95.50
N	5.16	4.47
Fe	0.14	0.03

Table S2. Comparison of CO_2 reduction performance of various catalysts

Catalysts	electrolyte	Potential (V vs. RHE)	FE_{CO} (%)	TOF (h^{-1})	Current density (mA cm^{-2})	Ref
Fe SAs	0.5 M $KHCO_3$	-0.9	99.46	12056	39.79	This work
7.6 Fe NPs	0.5 M $KHCO_3$	-0.9	92.05	1660	21.91	This work
16.7 Fe NPs	0.5 M $KHCO_3$	-0.9	82.78	273	14.40	This work
44.8 Fe NPs	0.5 M $KHCO_3$	-0.9	75.58	143	11.34	This work
Fe SAs	0.1 M $KHCO_3$	-0.6	80	/	1.75	[1]
Fe-N-C	0.1 M$NaHCO_3$	-0.6	91	/	7.5	[2]
Ni-N-C	0.1 M $KHCO_3$	-0.75	96	1060	8.2	[3]
Fe-NS-C	0.5 M $KHCO_3$	-0.6	98	/	7.1	[4]
Au Nanowires	0.5 M $KHCO_3$	-0.35	94	72	8.16	[5]
Co−N_5/ HNPCSs	0.2 M $NaHCO_3$	-0.73	99.2	480.2	~ 4.5	[6]
Nanoporous Ag	0.5 M $KHCO_3$	-0.5	92	7.2	~8.7	[7]
Pd Nanoparticles	0.1 M $KHCO_3$	-0.89	91	576	~9.76	[8]
Cu/SnO_2 NP	0.5 M $KHCO_3$	-0.7	93	/	4.6	[9]
Cu-Pd NPs	0.1 M $KHCO_3$	-0.9	87	/	47 mA $mgPd^{-1}$	[10]
ZnN_x/C	0.5 M $KHCO_3$	-0.43	95	1416	4.8	[11]
Ag-Cu aerogel	0.1 M $KHCO_3$	-0.89	89.40	/	5.86	[12]
Perfluorinated CoPc	0.5 M $KHCO_3$	-0.8	93	5760	~4.4	[13]

Table S3. The results of operando XAS

Sample	Coordination	CN	R(Å)	$\sigma^2(\times10^{-3}Å^2)$	ΔE(eV)	R-factor
Fe foil	Fe-Fe	8	2.46	/	/	/
	Fe-Fe	6	2.86	/	/	
Fe_2O_3	Fe-O	3	1.95	/	/	/
	Fe-O	3	2.12	/	/	
Dry	Fe-Fe	3.8	2.83	9.0	2.1	0.45%
	Fe-N	5.3	1.99	3.0	2.8	
	Fe-C	3.1	2.99	13.0	5.0	
-0.3V	Fe-N	5.4	2.01	3.0	2.4	0.22%
	Fe-C	1.4	3.03	10.0	5.0	
-0.8V	Fe-N	5.0	2.04	14.3	1.3	2.00%
	Fe-C	4.0	3.20	9.0	6.5	
-0.9V	Fe-N	2.4	1.93	3.0	-6.3	1.95%
	Fe-Fe	2.8	2.70	4.0	-1.9	

Reference

(1) Zhang, C.; Yang, S.; Wu, J.; Liu, M.; Yazdi, S.; Ren, M.; Sha, J.; Zhong, J.; Nie, K.; Jalilov, A. S.; Li, Z.; Li, H.; Yakobson, B. I.; Wu, Q.; Ringe, E.; Xu, H.; Ajayan, P. M.; Tour, J. M. Electrochemical CO2 Reduction with Atomic Iron-Dispersed on Nitrogen-Doped Graphene. *Advanced Energy Materials* **2018**, *8*.

(2) Huan, T. N.; Ranjbar, N.; Rousse, G.; Sougrati, M.; Zitolo, A.; Mougel, V.; Jaouen, F.; Fontecave, M. Electrochemical Reduction of CO2 Catalyzed by Fe-N-C Materials: A Structure–Selectivity Study. *ACS Catalysis* **2017**, *7*, 1520-1525.

(3) Pan, F.; Deng, W.; Justiniano, C.; Li, Y. Identification of champion transition metals centers in metal and nitrogen-codoped carbon catalysts for CO2 reduction. *Applied Catalysis B: Environmental* **2018**, *226*, 463-472.

(4) Pan, F.; Li, B.; Sarnello, E.; Hwang, S.; Gang, Y.; Feng, X.; Xiang, X.; Adli, N. M.; Li, T.; Su, D.; Wu, G.; Wang, G.; Li, Y. Boosting CO2 reduction on Fe-N-C with sulfur incorporation: Synergistic electronic and structural engineering. *Nano Energy* **2020**, *68*.

(5) Zhu, W.; Zhang, Y. J.; Zhang, H.; Lv, H.; Li, Q.; Michalsky, R.; Peterson, A. A.; Sun, S. Active and selective conversion of CO2 to CO on ultrathin Au nanowires. *J Am Chem Soc* **2014**, *136*, 16132-16135.

(6) Pan, Y.; Lin, R.; Chen, Y.; Liu, S.; Zhu, W.; Cao, X.; Chen, W.; Wu, K.; Cheong, W. C.; Wang, Y.; Zheng, L.; Luo, J.; Lin, Y.; Liu, Y.; Liu, C.; Li, J.; Lu, Q.; Chen, X.; Wang, D.; Peng, Q.; Chen, C.; Li, Y. Design of Single-Atom Co-N5 Catalytic Site: A Robust Electrocatalyst for CO2 Reduction with Nearly 100% CO Selectivity and Remarkable Stability. *J Am Chem Soc* **2018**, *140*, 4218-4221.

(7) Lu, Q.; Rosen, J.; Zhou, Y.; Hutchings, G. S.; Kimmel, Y. C.; Chen, J. G.; Jiao, F. A selective and efficient electrocatalyst for carbon dioxide reduction. *Nat Commun* **2014**, *5*, 3242.

(8) Gao, D.; Zhou, H.; Wang, J.; Miao, S.; Yang, F.; Wang, G.; Wang, J.; Bao, X. Size-dependent electrocatalytic reduction of CO2 over Pd nanoparticles. *J Am Chem Soc* **2015**, *137*, 4288-4291.

(9) Li, Q.; Fu, J.; Zhu, W.; Chen, Z.; Shen, B.; Wu, L.; Xi, Z.; Wang, T.; Lu, G.; Zhu, J. J.; Sun, S. Tuning Sn-Catalysis for Electrochemical Reduction of CO2 to CO via the Core/Shell Cu/SnO2 Structure. *J Am Chem Soc* **2017**, *139*, 4290-4293.

(10) Mun, Y.; Lee, S.; Cho, A.; Kim, S.; Han, J. W.; Lee, J. Cu-Pd alloy nanoparticles as highly selective catalysts for efficient electrochemical reduction of CO2 to CO. *Applied Catalysis B: Environmental* **2019**, *246*, 82-88.

(11) Yang, F.; Song, P.; Liu, X.; Mei, B.; Xing, W.; Jiang, Z.; Gu, L.; Xu, W. Highly Efficient CO2 Electroreduction on ZnN4 -based Single-Atom Catalyst. *Angew Chem Int Ed Engl* **2018**, *57*, 12303-12307.

(12) Wang, W.; Gong, S.; Liu, J.; Ge, Y.; Wang, J.; Lv, X. Ag-Cu aerogel for electrochemical CO2 conversion to CO. *J Colloid Interface Sci* **2021**, *595*, 159-167.

(13) Morlanés, N.; Takanabe, K.; Rodionov, V. Simultaneous Reduction of CO2 and Splitting of H2O by a Single Immobilized Cobalt Phthalocyanine Electrocatalyst. *ACS Catalysis* **2016**, *6*, 3092-3095.